

Domain-Wall *p-n* Junction in Lithium Niobate Thin Film on an Insulator

Yuezha Qian, Yuchen Zhang, Jingjun Xu[✉], and Guoquan Zhang^{✉*}

The MOE Key Laboratory of Weak-Light Nonlinear Photonics, School of Physics and TEDA Applied Physics Institute, Nankai University, Tianjin 300457, China



(Received 12 October 2021; revised 16 March 2022; accepted 21 March 2022; published 6 April 2022)

Domain-wall nanoelectronics has attracted extensive attention since the discovery of conductive domain walls, where domain-wall *p-n* junctions are indispensable for device applications. Here, we report on the fabrication of a domain-wall *p-n* junction based on *n*-type and *p*-type conductive domain walls in an *x*-cut lithium niobate thin film on an insulator using a lateral-electric-field poling technique. The electron and hole mobilities in the *n*-type and *p*-type domain walls are measured to be 337 and 93 cm² V⁻¹ s⁻¹, respectively, more than 400 times higher than those in the parent bulk crystal. The successful fabrication of a domain-wall *p-n* junction with large electron and hole mobilities in the domain walls makes lithium niobate on an insulator a promising platform for domain-wall nanoelectronics and optoelectronics.

DOI: 10.1103/PhysRevApplied.17.044011

I. INTRODUCTION

A ferroelectric domain wall (DW) is an ultrathin interface between two ferroelectric domains with different polarizations [1]. DWs can be intentionally created, moved, and erased under external fields [2,3], and can have very different properties from their parent materials; therefore, they are attracting extensive attention from both fundamental and technical points of view [1,4,5]. Although the parent material itself is insulating, charged DWs, formed due to a discontinuity in the spontaneous polarization \mathbf{P}_s at the DW, have been found to be conductive in various materials, such as BiFeO₃ [6,7], Pb(Zr_{0.2}Ti_{0.8})O₃ [8,9], BaTiO₃ [10], ErMnO₃ [11], HoMnO₃ [12,13], and LiNbO₃ [14,15], to mention just a few. In general, a DW is ultrathin, on the nanometer scale [16–18]; therefore, a conductive domain wall (CDW) forms a nanoscale conducting channel embedded in an insulating background, which is promising for nanoelectronics. Potential applications such as resistive switches [19,20] and memories [21–23] have been demonstrated based on CDWs. It is well known that the *p-n* junction is an indispensable fundamental element in modern optoelectronics. While the concept of *p-n* junctions along ferroelectric domain walls was employed by Zhang *et al.* [24] to explain the anisotropic polarization-induced conductance at the interface of a BiFeO₃-TbScO₃ heterostructure, up to now, a direct demonstration of a *p-n* junction is still lacking in DW nanoelectronics and optoelectronics.

Ideally, lithium niobate (LiNbO₃, LN) has 180° kink-type DWs, but in practice an inclination angle θ of the DW with respect to the spontaneous polarization \mathbf{P}_s can be created, resulting in a bound charge density proportional

to $2P_s \sin \theta$. A DW can be conductive with a nonzero inclination angle θ [14,15,20,25–29], where the bound charges in the DW are compensated for by free conducting electrons or holes, since there are no mobile ionized donors or defects at room temperature in LN [30,31]. Both “head-to-head” and “tail-to-tail” DWs have been observed experimentally; in most cases only the conductivity in the head-to-head DWs has been found to be significantly increased by several orders of magnitude as compared with that of a bulk single-domain crystal [5,15,20,25,28], unlike the tail-to-tail DWs, which usually exhibit insulating behavior [20,25,28], most probably due to the small inclination angle, as predicted theoretically by Eliseev *et al.* based on the Landau-Ginzburg-Devonshire theory [32]. It is known that the key to control the conductivity of CDWs in LN is controlling the inclination angle of the DWs [32], which is of essential importance for understanding the charge transport properties and for device design. However, up to now, it is still challenging to precisely control the inclination angle of a single DW, and in most cases the inclination angle is small and less than approximately 5° [15,20,25,27,29]. An inclination angle $\theta = 20^\circ$ was reported in a head-to-head DW [28], and samples with head-to-head DWs with an inclination angle $\theta = 90^\circ$ were also prepared by heating the crystal close to the Curie temperature of LN (approximately 1100 °C), followed by a slower cooling-down process [33,34], but the DW quality was not good enough to increase the conductivity as expected [34]. In addition, the polarity of the conducting majority carrier in DWs in LN has not yet been identified directly, which is also of fundamental importance in the context of the charge transport behavior in DWs and practical applications of DW-based devices.

In this paper, we propose a lateral-electric-field poling scheme to fabricate head-to-head and tail-to-tail CDWs

* zhangqq@nankai.edu.cn

with an arbitrary predesigned inclination angle on x -cut or y -cut LN thin films on an insulator (LNOI). The conducting majority carriers in the head-to-head and tail-to-tail CDWs are identified to be electrons and holes, respectively, through Hall measurements. The electron and hole mobilities in the CDWs in LN are found to be within the range for typical wide-band-gap semiconductors. Most importantly, a p - n junction, the fundamental element of optoelectronic devices, is fabricated successfully based on CDWs in LNOI with perfect rectifying features, which paves the way for practical DW nanoelectronic and optoelectronic devices based on LNOI.

II. CHARACTERIZATION OF DW CONDUCTION PROPERTIES

A. Preparation of head-to-head and tail-to-tail DWs

We use a lateral-electric-field poling scheme to fabricate head-to-head and tail-to-tail DWs in x -cut or y -cut LNOI. The x -cut LNOI samples (commercially available from NANOLN, Jinan, China) have a layered structure composed of a 600-nm x -cut LN thin film (doped with 5.0 mol% MgO), a 2- μm silica layer, and a 500- μm LN substrate that are bonded in sequence [35]. The spontaneous polarization \mathbf{P}_s of the x -cut LN thin film lies in the surface plane of the sample. To invert the spontaneous polarization in the x -cut LN thin film, we deposit a set of interdigital electrodes on the top surface of the LN film by employing a lithographic magnetron sputtering technique. Figure 1(a) shows a schematic diagram of typical interdigital electrodes on the LNOI surface, and Fig. 1(b) shows an enlargement of a typical unit cell composed of a pair of electrodes, in which the gap between the two electrodes a and b is d , and the width of both electrodes is w_e . The crossing angle between \mathbf{P}_s and the long edges of the electrodes a and b , i.e., the inclination angle of the DW, is θ , so that when one applies an external electric field E_p to the interdigital electrodes with the electrodes a and b being the positive and negative electrodes, respectively, the effective in-plane poling field required to invert the spontaneous polarization of the x -cut LN thin film is $E_p \sin \theta$, i.e., the external field component antiparallel to the spontaneous polarization \mathbf{P}_s . It has been reported that, for a z -cut LN crystal with a MgO doping concentration of 5.0 mol%, the coercive field is around 4.5 kV mm^{-1} [36]. However, we find that, for the case of x -cut LNOI with the lateral-electric-field poling scheme, the in-plane poling field required to invert \mathbf{P}_s within the surface plane is around 40 kV mm^{-1} , much higher than that for z -cut LN. This is mainly due to the fact that the x -cut LN thin film is bonded to the underlying silica layer, which impedes domain inversion. The strong poling field also ensures complete domain inversion throughout the depth of the LN thin film, in good accordance with a previous report [37]. With the interdigital electrodes shown in Fig. 1(a)

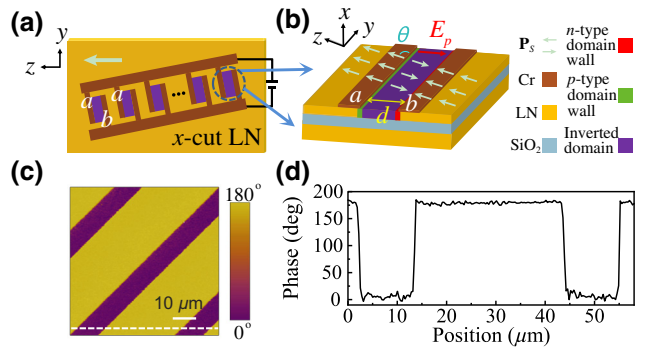


FIG. 1. Preparation of head-to-head and tail-to-tail DWs in x -cut LNOI. (a) Schematic diagram of the experimental setup to pole x -cut LN with a set of 500-nm-thick Cr interdigital electrodes deposited on the top surface of the LNOI. The purple areas are inverted domains with a spontaneous polarization \mathbf{P}_s antiparallel to the original polarization of the x -cut LNOI. (b) Enlargement of unit cell shown in (a), forming a typical p - i - n -type p - n junction. (c) PFM phase image of periodically poled x -cut LNOI with $\theta = 45^\circ$. The period of the periodically poled LNOI is $30 \mu\text{m}$, and the width of the inverted domain is $8 \mu\text{m}$. (d) Phase profile of the periodically poled LNOI along the white dashed line in (c).

and appropriate polarity of the poling field, \mathbf{P}_s of the purple area in Figs. 1(a) and 1(b) is inverted (details of the poling can be found in the Appendix), and the DW is located just along the long edge of the electrodes, as also confirmed by the piezoresponse-force-microscopy (PFM) images of the domain pattern shown in Figs. 1(c) and 1(d). In this way, both head-to-head and tail-to-tail DWs with an arbitrary predesigned inclination angle θ can be precisely fabricated. Similar results can also be obtained for the y -cut LNOI samples, but the following results are mainly based on the x -cut LNOI.

The lateral-electric-field poling scheme for fabricating CDWs in x -cut and y -cut LNOI has the following advantages. First, one can produce both head-to-head and tail-to-tail CDWs with enhanced n -type and p -type conductivity, as we show in Sec. II B, and the inclination angle of both types of CDW can be precisely controlled to an arbitrary predesigned value up to 90° . Second, all electrodes are in-plane and are deposited on the top surface of the LNOI, which is easy to operate on, and complicated DW-based optoelectronic devices or circuits can be designed conveniently. Third, a bottom electrode, which is usually required in the domain inversion of z -cut LNOI, is avoided. This is beneficial for photonic applications because the bottom metal electrode usually has strong light absorption, resulting in a large light-propagation loss.

B. Measurement of DW conductivity

The electrical conductivity of the head-to-head and tail-to-tail CDWs is measured using the experimental setup schematically shown in Fig. 2(a). Here, we prepare 20 pairs

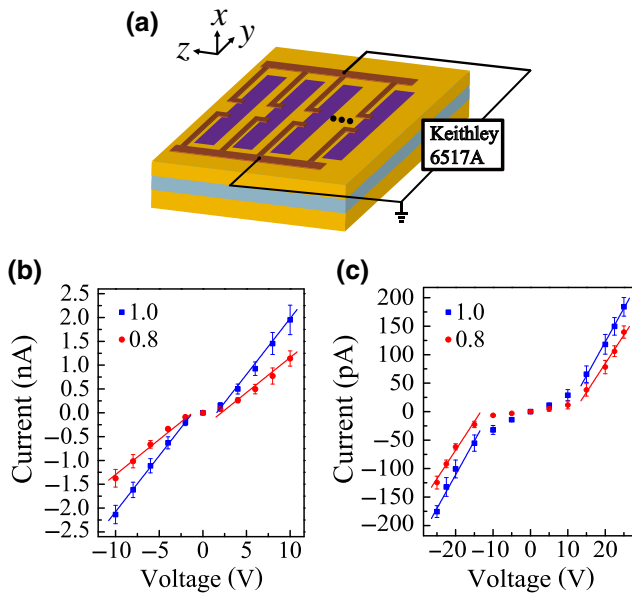


FIG. 2. Measurement of the I - V curves of head-to-head and tail-to-tail CDWs. (a) Schematic diagram of the experimental setup to measure the I - V curves of the CDWs. (b),(c) Measured I - V curves of 20 parallel-connected head-to-head CDWs and 20 parallel-connected tail-to-tail CDWs, respectively, for different inclination angles with $\sin \theta = 0.8$ and 1.0. The error bars are the standard errors of the measurement data, and the lines are linear fits to the experimental data in both cases.

of head-to-head and tail-to-tail CDWs using the interdigital electrodes to pole the x -cut LNOI, as described above in Sec. II A, showing the high efficiency and reproducibility of the poling technique. Then, the interdigital Cr electrodes are removed using a Cr etchant, while the LN film is unaffected, since LN is immune to the Cr etchant. After that, pairs of new 300-nm-thick Cr electrodes, each pair of electrodes covering the same CDW, as shown in Fig. 2(a), are deposited on the surface of the periodically poled x -cut LNOI. For the head-to-head CDWs, the gap between the positive and negative electrodes L is set to $7 \mu\text{m}$, while the electrode gap for the tail-to-tail CDWs is set to $L = 3 \mu\text{m}$. This is because the conductivity of the tail-to-tail CDWs is found to be much smaller than that of the head-to-head CDWs, and a smaller electrode gap is beneficial for obtaining a larger current. The current-voltage (I - V) curves of the CDWs are then measured with an ammeter (Keithley 6517A), which also provides the applied electrical voltage.

Figures 2(b) and 2(c) show the measured I - V curves for 20 parallel-connected head-to-head and tail-to-tail CDWs, respectively, for different inclination angles θ . One sees that the I - V curves exhibit a double-sided slightly diodelike behavior for both types of CDWs, indicating that the Cr-LN contact is not perfectly Ohmic. The I - V curves are linear in the voltage range beyond the central double-sided diodelike area, from which the DW conductivity is calculated through the formula $\sigma_{e,h} = S_{I-V}L/(mS_{DW})$ in

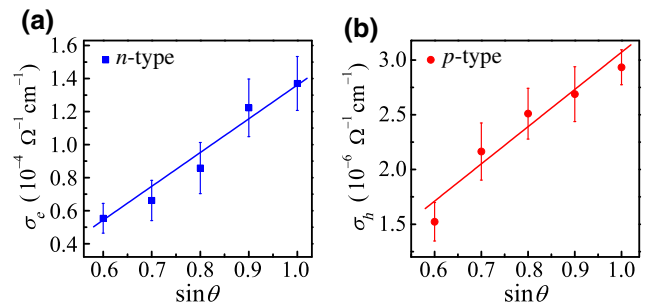


FIG. 3. Measurements of the DW conductivity (a) σ_e for the head-to-head CDWs and (b) σ_h for the tail-to-tail CDWs, for different inclination angles θ . The error bars are the standard errors of the measurement data, and the lines are linear fits to the experimental data in both cases.

both cases, where S_{I-V} is the slope of the I - V curve in Fig. 2(b) or 2(c) far away from the central double-sided diodelike part, L is the gap distance between the two electrodes, $m = 20$ is the number of CDWs connected in parallel, and S_{DW} is the cross-sectional area of a single CDW, equal to the product of the CDW width $w_{DW} = 10 \text{ nm}$ [15,18] and the CDW depth $d_{DW} = 600 \text{ nm}$. For example, the conductivity is measured to be $\sigma_e = 1.36 \times 10^{-4} \Omega^{-1} \text{cm}^{-1}$ for the head-to-head CDWs and $\sigma_h = 2.93 \times 10^{-6} \Omega^{-1} \text{cm}^{-1}$ for the tail-to-tail CDWs when the inclination angle θ is set to 90° . One sees that the DW conductivity, for both the head-to-head and the tail-to-tail DWs, is enhanced by at least 6 orders of magnitude compared with that of the parent single-domain MgO-doped LN thin film, which is lower than $10^{-12} \Omega^{-1} \text{cm}^{-1}$, the accuracy of our measurement system. Note that the successful fabrication of tail-to-tail DWs with enhanced conductivity benefits from the capability to fabricate DWs with a large inclination angle θ . In previous reports, the inclination angle of the tail-to-tail DWs was too small to have an enhanced conductivity, due to the low concentration of conducting holes [29,32].

The dependence of the DW conductivity on the inclination angle θ is shown in Figs. 3(a) and 3(b). As expected, the conductivity increases linearly with an increase in $\sin \theta$, in good agreement with the theoretical prediction for the DW conductivity in LN crystals [32].

C. Hall measurement

It is well known that there are no mobile ionized donors or defects at room temperature in LN [30–32]; therefore, electrons and holes are the conducting majority carriers in head-to-head and tail-to-tail CDWs, respectively, in LN. This is confirmed experimentally by Hall-measurement results. Figure 4 shows a schematic diagram of the experimental setup to measure the Hall voltage of the CDWs. Here, we prepare 20 head-to-head CDWs and 20 tail-to-tail CDWs, using the lateral-electric-field poling technique and the poling setup shown in Fig. 1(a). Then, the interdigital

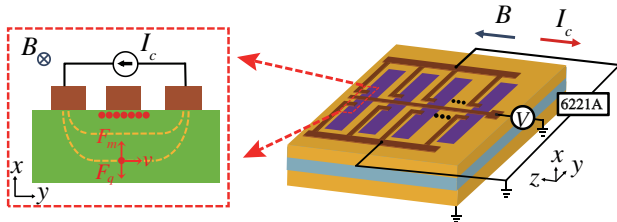


FIG. 4. Schematic diagram of the experimental setup to measure the Hall voltage of CDWs. Here, B is the externally applied magnetic field, and I_c is a constant current provided by the Keithley 6221A instrument. The inset shows the x - y cross-sectional plane parallel to the CDW, which illustrates the mechanism of the use of the Hall effect to determine the polarity of conducting majority carriers. Here, F_m , F_q , and v are the Lorentz force, the Coulomb force, and the velocity of conducting majority carriers, respectively.

Cr poling electrodes are removed using the Cr etchant, while the LNOI is unaffected by the Cr etchant. After that, two 300-nm-thick Cr electrodes with a gap distance of $20\ \mu\text{m}$ are deposited on each head-to-head (or tail-to-tail) CDW, and all head-to-head (or tail-to-tail) CDWs are connected in parallel. An additional Cr electrode, with a width of $10\ \mu\text{m}$, covering all head-to-head (or tail-to-tail) CDWs is deposited in the middle of two lateral electrodes to measure the Hall voltage. A magnetic field B is applied along the z axis of the experimental coordinates, with $+B$ being along the $+z$ axis and $-B$ being along the $-z$ axis, and a constant current I_c provided by the Keithley 6221A instrument is injected into the parallel-connected CDWs in the $+y$ -axis direction. The inset shows the x - y cross-sectional plane parallel to the CDW, which illustrates the mechanism of the use of the Hall effect to determine the polarity of the conducting majority carriers [38], where F_m , F_q , and v are the Lorentz force, the Coulomb force, and the velocity of the conducting majority carriers, respectively. With a magnetic field B along the $+z$ axis and an injected current I_c along the $+y$ axis, electrons should be the conducting majority carriers in the CDW if the Hall voltage V_H is negative, while holes are the conducting majority carriers if the Hall voltage is positive.

Figure 5 shows the measured dependence of the Hall voltage V_H on the externally applied magnetic field B for both the head-to-head and the tail-to-tail CDWs with an inclination angle $\theta = 90^\circ$. Here, the magnetic field B is applied along the $+z$ axis, a constant current I_c is injected into 20 parallel-connected CDWs along the $+y$ axis, and the Hall voltage V_H is measured in the x -axis direction of the experimental coordinate system shown in Fig. 4. When the top surface of the x -cut LNOI in Fig. 4 is negatively charged, the Hall voltage V_H is negative, and electrons are the conducting majority carriers. When the Hall voltage V_H is positive, holes are the conducting majority carriers. In addition, we confirm experimentally that the polarity

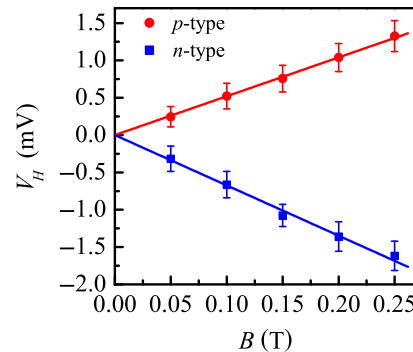


FIG. 5. Dependence of the Hall voltage V_H on the magnetic field B with a constant current I_c for the head-to-head and tail-to-tail CDWs. Here, 20 parallel-connected head-to-head (or tail-to-tail) CDWs with an inclination angle $\theta = 90^\circ$ are prepared. The constant current I_c is injected into the 20 parallel-connected CDWs. The lines are linear fits to the measurement data, and the error bars are the standard errors of the measurement data.

of the Hall voltage is reversed when the direction of the magnetic field is reversed while the constant current is kept unchanged. These results clearly demonstrate that the head-to-head CDWs have n -type conductivity and the tail-to-tail CDWs have p -type conductivity. For comparison, we also try to perform a Hall measurement on the parent LN film itself but do not get any reliable signal, because the conductivity of the parent LN film is too small (less than $10^{-12}\ \Omega^{-1}\text{cm}^{-1}$).

One can also obtain the concentration of conducting electrons n_e (or holes, n_h) in the n -type (or p -type) CDWs from the Hall-measurement results through the formula $n_{e,h} = I_c/(qms_Hw_{DW})$, where q is the elementary charge of electrons and holes, m is the number of parallel-connected CDWs in the Hall-voltage measurement, $S_H = V_H/B$ is the slope of the V_H - B curves in Fig. 5, and w_{DW} is the width of a single CDW. By substituting the experimental parameters $m = 20$, $I_c = 0.43\ \text{nA}$, $S_H = 5.33\ \text{mV T}^{-1}$, and $w_{DW} = 10\ \text{nm}$ [15,18] into the formula, the conducting-electron concentration n_e is calculated to be $2.52 \times 10^{12}\ \text{cm}^{-3}$ in the n -type CDWs. Similarly, by substituting the experimental parameters $m = 20$, $I_c = 42\ \text{pA}$, $S_H = 6.65\ \text{mV T}^{-1}$, and $w_{DW} = 10\ \text{nm}$ into the formula, one can obtain the conducting-hole concentration $n_h = 1.97 \times 10^{11}\ \text{cm}^{-3}$ in the p -type CDWs.

Furthermore, one can also estimate the mobility of electrons (μ_e) and holes (μ_h) in the n -type and p -type CDWs, respectively, via the formula $\mu_{e,h} = \sigma_{e,h}/(qn_{e,h})$. For example, for the cases of n -type and p -type CDWs with an inclination angle $\theta = 90^\circ$, and with the measured $\sigma_e = 1.36 \times 10^{-4}\ \Omega^{-1}\text{cm}^{-1}$, $n_e = 2.52 \times 10^{12}\ \text{cm}^{-3}$, $\sigma_h = 2.93 \times 10^{-6}\ \Omega^{-1}\text{cm}^{-1}$, and $n_h = 1.97 \times 10^{11}\ \text{cm}^{-3}$, the electron and hole mobilities are calculated to be $\mu_e = 337.30\ \text{cm}^2\text{V}^{-1}\text{s}^{-1}$ and $\mu_h = 92.96\ \text{cm}^2\text{V}^{-1}\text{s}^{-1}$, respectively, which are more than 400 times larger than

the electron mobility of $0.8 \text{ cm}^2 \text{ V}^{-1} \text{ s}^{-1}$ in reduced bulk LN crystals [39], and are within the range for typical wide-band-gap semiconductors. Note that the DW conductivity in LNOI is dependent not only the DW inclination angle θ but also on defects, including stoichiometry-related intrinsic defects and dopant-related extrinsic defects, and their concentrations in the LN thin film. For example, doping the film with Mg^{2+} ions increases the electrical conductivity of LN due to a decrease in antisite defects Nb_{Li} , which act as electron acceptors [30,31,40]. Especially, it is feasible to improve the *p*-type DW conductivity by doping LN with nitrogen [41,42]. Similarly to the case of the semiconductor Si, a lot of work is necessary to optimize the DW performance and to find the most appropriate dopant and stoichiometry for specific device applications.

III. *p-n* JUNCTION

The capability to produce both *n*-type and *p*-type CDWs in the same *x*-cut LNOI, no matter whether the parent LNOI is *n*-type or *p*-type, makes the fabrication of *p-n* junctions possible. Indeed, the unit cell shown in Fig. 1(b), composed of a *p*-type CDW, an intermediate thin region of LN with a width d , and an *n*-type CDW, forms a typical *p-i-n*-type *p-n* junction [43]. It should be noted that, for a DW *p-n* junction, the polarity of the majority carriers in the DW is determined by and opposite to the polarity of the bound charges induced by the discontinuity in the spontaneous polarization of the DW, while the concentration of the majority carriers is dependent on both the dopant and the density of bound charges, related to the inclination angle θ . This is very different from the case of traditional semiconductors, where both the polarity and the concentration of the majority carriers are determined solely by the dopants.

We measure the rectifying characteristics of the *p-i-n*-type *p-n* junctions under different conditions with a set of 20 parallel-connected *p-n* junctions prepared using the interdigital electrodes shown in Fig. 1(a). Since the conducting-majority-carrier concentration in CDWs is highest for an inclination angle $\theta = 90^\circ$, we first measure the *J-V* curve of the parallel *p-n* junctions for $\theta = 90^\circ$. The width of the intermediate thin LN region, i.e., the distance between the *p*-type CDW and the *n*-type CDW, is set to $d = 6.5 \mu\text{m}$, and the length of the intermediate LN, i.e., the length of the *p*-type or *n*-type CDW, is $100 \mu\text{m}$. The *J-V* curve of the parallel *p-n* junctions is shown in Fig. 6(a). One sees that the *p-n* junctions demonstrate typical rectifying features, showing perfect unidirectional conduction behavior. The *p-n* junctions are conductive under a forward bias, and the electric current density J increases exponentially with an increase in the forward bias voltage, following the formula $J = J_s[\exp(qV/\beta k_B T) - 1]$, where J_s is the reverse saturation current density, β is the ideality factor, k_B is the Boltzmann constant, and T is the absolute

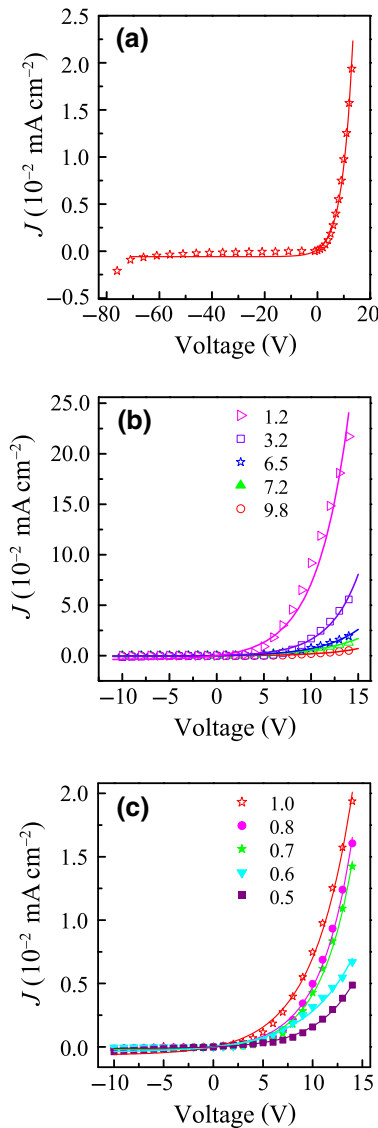


FIG. 6. Measurement of the rectifying *J-V* curves of 20 parallel-connected DW *p-n* junctions under various conditions. (a) *J-V* curve of DW *p-n* junctions for an inclination angle $\theta = 90^\circ$ and an intermediate LN width $d = 6.5 \mu\text{m}$. (b) *J-V* curves of DW *p-n* junctions with intermediate LN widths $d = 1.2, 3.2, 6.5, 7.2$, and $9.8 \mu\text{m}$. The inclination angle θ is 90° . (c) *J-V* curves of DW *p-n* junctions for different inclination angles with $\sin \theta = 0.5, 0.6, 0.7, 0.8$, and 1.0 . The intermediate LN width d is $6.5 \mu\text{m}$. The length of the *n*-type and *p*-type CDWs is $100 \mu\text{m}$ in all cases. The curves in all cases are exponential fits to the measured data according to the formula $J = J_s[\exp(qV/\beta k_B T) - 1]$, and the fitting parameters can be found in Table I.

temperature in kelvin [43,44]. Typical fitting parameters for the case in Fig. 6(a) are $\beta = 150$ and $J_s = 5.9 \times 10^{-4} \text{ mA cm}^{-2}$, at room temperature ($T = 300 \text{ K}$). Note that the ideality factor β is very large in general; this is typical for wide-band-gap materials, indicating a tunneling charge transport mechanism rather than thermal diffusion [44]. On the other hand, the *p-n* junctions are resistively

interrupted under a reverse bias, and the reverse saturation current density J_s is negligibly small until the p - n junctions break down, at which point the current increases suddenly. The reverse-biased breakdown voltages of the p - n junctions are measured to be approximately 70 V. It should be noted that the measured I - V curves of both the n -type head-to-head DWs and the p -type tail-to-tail DWs are symmetric [see Figs. 2(b) and 2(c)]; this justifies the conclusion that the observed rectifying behavior of the p - n junction is not due to a Schottky barrier.

We find that the rectifying features of the p - i - n -type DW p - n junctions appear only when the width d of the intermediate LN region is small enough. Figure 6(b) shows the J - V curves of 20 parallel-connected p - n junctions with different intermediate LN widths d . The inclination angle θ is set to 90°, and the length of the p -type and n -type CDWs is 100 μm in all cases. One sees that the rectifying performance of the DW p - n junctions is better for a smaller width d , and the rectifying features disappear when the width d is larger than approximately 10 μm. This is understandable because the tunneling rate of electrons and holes decreases with an increase in the width d , and finally there is no tunneling when the width d is large enough that the DW p - n junction becomes resistively interrupted.

The rectifying performance of the DW p - n junctions is also dependent on the concentrations of conducting majority carriers in the n -type and p -type CDWs; therefore, it should also be dependent on the inclination angle θ . Figure 6(c) shows the measured J - V curves of 20 parallel-connected p - n junctions for different inclination angles θ . Again, the width and length of the intermediate LN region are set to 6.5 μm and 100 μm, respectively. One sees that the rectifying current under a forward bias becomes large with an increase in the inclination angle θ , i.e., an increase in the concentrations of conducting electrons and holes in the n -type and p -type CDWs. As expected, the rectifying performance of the DW p - n junctions is best at $\theta = 90^\circ$. Note that in all the above cases

TABLE I. Fitting parameters for the measured J - V data in Fig. 6 with the exponential formula $J = J_s[\exp(qV/\beta k_B T) - 1]$. The other parameters are the room temperature $T = 300$ K, the elementary charge $q = 1.6 \times 10^{-19}$ C, and the Boltzmann constant $k_B = 1.38 \times 10^{-23}$ JK⁻¹.

$\sin \theta$	d (μm)	β	J_s (10 ⁻⁴ mA cm ⁻²)
1.0	9.8	147	1.3
1.0	7.2	187	8.1
1.0	6.5	150	5.9
1.0	3.2	122	7.1
1.0	1.2	159	3.9
0.8	6.5	126	2.4
0.7	6.5	125	2.0
0.6	6.5	186	4.1
0.5	6.5	145	1.2

shown in Fig. 6 the rectifying J - V curves can be well fitted by the exponential formula $J = J_s[\exp(qV/\beta k_B T) - 1]$, with the fitting parameters being listed in Table I.

IV. CONCLUSION

In conclusion, we prepare both head-to-head and tail-to-tail CDWs with arbitrary predesigned inclination angles in x -cut or y -cut LNOI through a lateral-electric-field poling technique. Both head-to-head and tail-to-tail DWs are found to be conductive and are verified to have n -type and p -type conductivity, respectively, via Hall measurements, and the electron and hole mobilities are measured to be $\mu_e = 337$ cm² V⁻¹ s⁻¹ and $\mu_h = 93$ cm² V⁻¹ s⁻¹, respectively, which are within the range of those of typical wide-band-gap semiconductors. Based on these n -type and p -type CDWs, we successfully fabricate a p - i - n -type p - n junction, demonstrating perfect rectifying conduction behavior. The p - n junction is a fundamental element in modern integrated optoelectronic circuits. The successful fabrication of DW p - n junctions, as well as the large electron and hole mobilities in DWs in LNOI, may pave the way for chip-level optoelectronic integration based on LNOI, which is a long-pursued goal in the scientific and industrial communities.

ACKNOWLEDGMENTS

The authors would like to thank Dr. Xiaojie Wang, Dr. Yuejian Jiao, Mr. Sanbing Li, and Ms. Meili Li from Nankai University for helpful discussions. This work is supported by the National Natural Science Foundation of China (NSFC) (Grants No. 12134007, No. 11774182, and No. 11734009), the National Key Research and Development Program of China (Grant No. 2019YFA0705000), the 111 project (Grant No. B07013), and the Tianjin Municipal Natural Science Foundation (Grant No. 21JCZDJC00150).

APPENDIX: POLING THE x -CUT LNOI WITH THE LATERAL-ELECTRIC-FIELD POLING TECHNIQUE

With the interdigital electrodes deposited on the x -cut LNOI [see Fig. 1(a)], one applies in-plane staged electric field pulses to invert the spontaneous polarization \mathbf{P}_s of the x -cut LN thin film. A whole staged electric field pulse consists of a prepoling stage, an effective poling stage, a domain-coalescing stage, and a domain-stabilization stage. In the prepoling stage, the effective poling field $E_p \sin \theta$ is increased to 30 kV mm⁻¹, lower than the coercive field of the x -cut LNOI, at a rate of 60 kV mm⁻¹ s⁻¹, and the field is kept constant for 500 ms. With this prepoling stage, the crystal tends to nucleate more easily in the subsequent effective poling stage. Then, the effective poling field is suddenly increased to 40 kV mm⁻¹ or higher and is kept

at this value for 200 ms in the effective poling stage to partially invert the domain polarization. After that, the effective poling field is dropped to 30 kV mm⁻¹ and kept constant for 500 ms, during which the partially inverted domains coalesce. Following this, the effective poling field is decreased to 12 kV mm⁻¹ at a rate of 90 kV mm⁻¹ s⁻¹ and kept constant for 3.0 s for domain stabilization, to prevent the inverted domain from flipping back, and then the field is decreased to zero at a rate of 40 kV mm⁻¹ s⁻¹. This domain in the *x*-cut LNOI can be completely inverted after around a dozen such staged electric field pulses, as confirmed by the PFM measurement shown in Fig. 1(c). The same poling procedure is applicable to *y*-cut LNOI.

The poling process has no effect on the surface of the LNOI. Figure 7 shows typical surface topographies of the LNOI before and after the poling process, measured by a scanning electron microscope (SEM), where the white arrows indicate the spontaneous polarization \mathbf{P}_s of the LN, and the red dashed boxes in Fig. 7(b) show the locations of the poling electrodes; the signs “+” and “-” represent the positive and negative poling electrodes, respectively. Note that the Cr poling electrodes are removed by the Cr etchant before the SEM measurement. The inset in Fig. 7(b) shows a magnified SEM image of the area within the blue box around the domain wall. The vertical grayish trace shows the position of the DW because the structure of the DW is different from that of the parent material.

The quality of the domain structures is characterized by PFM (MFP-3D Infinity, Asylum Research, Goleta, CA, USA) in the Dual AC Resonance Tracking and Switching

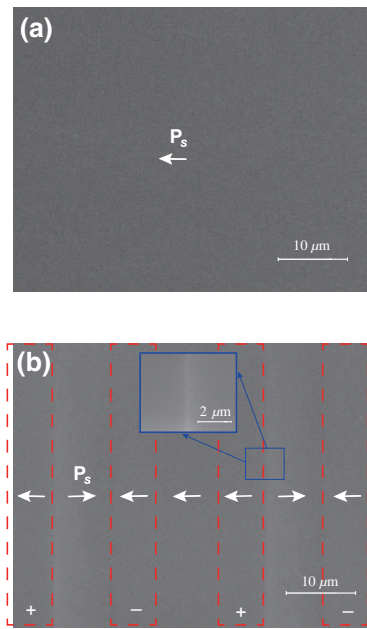


FIG. 7. SEM surface topographies of LNOI before (a) and after (b) the poling process. The inset in (b) shows a magnified SEM image of the area within the blue box around the DW.

Spectroscopy PFM (DART-SSPFM) lateral mode with a driving voltage of 3 V and a resonant frequency of 820 kHz; Ti/Ir-coated Si cantilevers with a force constant of 2.8 N m⁻¹ and a probe tip radius of 25 nm are used. Typical results are shown in Figs. 1(c) and 1(d).

- [1] V. Gopalan, V. Dierolf, and D. A. Scrymgeour, Defect–domain wall interactions in trigonal ferroelectrics, *Annu. Rev. Mater. Res.* **37**, 449 (2007).
- [2] L. McGilly, P. Yudin, L. Feigl, A. Tagantsev, and N. Setter, Controlling domain wall motion in ferroelectric thin films, *Nat. Nanotechnol.* **10**, 145 (2015).
- [3] J. R. Whyte and J. M. Gregg, A diode for ferroelectric domain-wall motion, *Nat. Commun.* **6**, 7361 (2015).
- [4] G. Catalan, J. Seidel, R. Ramesh, and J. F. Scott, Domain wall nanoelectronics, *Rev. Mod. Phys.* **84**, 119 (2012).
- [5] P. S. Bednyakov, B. I. Sturman, T. Sluka, A. K. Tagantsev, and P. V. Yudin, Physics and applications of charged domain walls, *npj Comput. Mater.* **4**, 65 (2018).
- [6] J. Seidel, L. W. Martin, Q. He, Q. Zhan, Y. H. Chu, A. Rother, M. E. Hawkridge, P. Maksymovych, P. Yu, M. Gajek, N. Balke, S. V. Kalinin, S. Gemming, F. Wang, G. Catalan, J. F. Scott, N. A. Spaldin, J. Orenstein, and R. Ramesh, Conduction at domain walls in oxide multiferroics, *Nat. Mater.* **8**, 229 (2009).
- [7] T. Rojac, A. Bencan, G. Drazic, N. Sakamoto, H. Ursic, B. Jancar, G. Tavcar, M. Makarovic, J. Walker, B. Malic, and D. Damjanovic, Domain-wall conduction in ferroelectric BiFeO₃ controlled by accumulation of charged defects, *Nat. Mater.* **16**, 322 (2017).
- [8] J. Guyonnet, I. Gaponenko, S. Gariglio, and P. Paruch, Conduction at domain walls in insulating Pb(Zr_{0.2}Ti_{0.8})O₃ thin films, *Adv. Mater.* **23**, 5377 (2011).
- [9] P. Maksymovych, A. N. Morozovska, P. Yu, E. A. Eliseev, Y.-H. Chu, R. Ramesh, A. P. Baddorf, and S. V. Kalinin, Tunable metallic conductance in ferroelectric nanodomains, *Nano Lett.* **12**, 209 (2011).
- [10] T. Sluka, A. Tagantsev, P. Bednyakov, and N. Setter, Free-electron gas at charged domain walls in insulating BaTiO₃, *Nat. Commun.* **4**, 1808 (2013).
- [11] D. Meier, J. Seidel, A. Cano, K. Delaney, Y. Kumagai, M. Mostovoy, N. A. Spaldin, R. Ramesh, and M. Fiebig, Anisotropic conductance at improper ferroelectric domain walls, *Nat. Mater.* **11**, 284 (2012).
- [12] W. Wu, Y. Horibe, N. Lee, S. W. Cheong, and J. R. Guest, Conduction of Topologically Protected Charged Ferroelectric Domain Walls, *Phys. Rev. Lett.* **108**, 077203 (2012).
- [13] W. Wu, J. R. Guest, Y. Horibe, S. Park, T. Choi, S. W. Cheong, and M. Bode, Polarization-Modulated Rectification at Ferroelectric Surfaces, *Phys. Rev. Lett.* **104**, 217601 (2010).
- [14] M. Schröder, A. Haußmann, A. Thiessen, E. Soergel, T. Woike, and L. M. Eng, Conducting domain walls in lithium niobate single crystals, *Adv. Funct. Mater.* **22**, 3936 (2012).
- [15] C. S. Werner, S. J. Herr, K. Buse, B. Sturman, E. Soergel, C. Razzaghi, and I. Breunig, Large and accessible conductivity

- of charged domain walls in lithium niobate, *Sci. Rep.* **7**, 9862 (2017).
- [16] C. L. Jia, S. B. Mi, K. Urban, I. Vrejoiu, M. Alexe, and D. Hesse, Atomic-scale study of electric dipoles near charged and uncharged domain walls in ferroelectric films, *Nat. Mater.* **7**, 57 (2008).
- [17] Y.-P. Chiu, Y.-T. Chen, B.-C. Huang, M.-C. Shih, J.-C. Yang, Q. He, C.-W. Liang, J. Seidel, Y.-C. Chen, R. Ramesh, and Y.-H. Chu, Atomic-scale evolution of local electronic structure across multiferroic domain walls, *Adv. Mater.* **23**, 1530 (2011).
- [18] J. Gonnissen, D. Batuk, G. F. Nataf, L. Jones, A. M. Abakumov, S. Van Aert, D. Schryvers, and E. K. H. Salje, Direct observation of ferroelectric domain walls in LiNbO_3 : Wall-meanders, kinks, and local electric charges, *Adv. Funct. Mater.* **26**, 7599 (2016).
- [19] J. A. Mundy, J. Schaab, Y. Kumagai, A. Cano, M. Stengel, I. P. Krug, D. M. Gottlob, H. Dog Anay, M. E. Holtz, R. Held, Z. Yan, E. Bourret, C. M. Schneider, D. G. Schlom, D. A. Muller, R. Ramesh, N. A. Spaldin, and D. Meier, Functional electronic inversion layers at ferroelectric domain walls, *Nat. Mater.* **16**, 622 (2017).
- [20] B. Kirbus, C. Godau, L. Wehmeier, H. Beccard, E. Beyreuther, A. Haußmann, and L. M. Eng, Real-time 3D imaging of nanoscale ferroelectric domain wall dynamics in lithium niobate single crystals under electric stimuli: Implications for domain-wall-based nanoelectronic devices, *ACS Appl. Nano Mater.* **2**, 5787 (2019).
- [21] P. Sharma, Q. Zhang, D. Sando, C. Lei, Y. Liu, J. Li, V. Nagarajan, and J. Seidel, Nonvolatile ferroelectric domain wall memory, *Sci. Adv.* **3**, e1700512 (2017).
- [22] J. Jiang, Z. L. Bai, Z. H. Chen, L. He, D. W. Zhang, Q. H. Zhang, J. A. Shi, M. H. Park, J. F. Scott, C. S. Hwang, and A. Q. Jiang, Temporary formation of highly conducting domain walls for non-destructive read-out of ferroelectric domain-wall resistance switching memories, *Nat. Mater.* **17**, 49 (2018).
- [23] J. Ma, J. Ma, Q. Zhang, R. Peng, J. Wang, C. Liu, M. Wang, N. Li, M. Chen, X. Cheng, P. Gao, L. Gu, L. Q. Chen, P. Yu, J. Zhang, and C. W. Nan, Controllable conductive read-out in self-assembled, topologically confined ferroelectric domain walls, *Nat. Nanotechnol.* **13**, 947 (2018).
- [24] Y. Zhang, H. Lu, L. Xie, X. Yan, T. R. Paudel, J. Kim, X. Cheng, H. Wang, C. Heikes, L. Li, M. Xu, D. G. Schlom, L. Q. Chen, R. Wu, E. Y. Tsymbal, A. Gruverman, and X. Pan, Anisotropic polarization-induced conductance at a ferroelectric-insulator interface, *Nat. Nanotechnol.* **13**, 1132 (2018).
- [25] C. Godau, T. Kampfe, A. Thiessen, L. M. Eng, and A. Haußmann, Enhancing the domain wall conductivity in lithium niobate single crystals, *ACS Nano* **11**, 4816 (2017).
- [26] T. R. Volk, R. V. Gainutdinov, and H. H. Zhang, Domain-wall conduction in AFM-written domain patterns in ion-sliced LiNbO_3 films, *Appl. Phys. Lett.* **110**, 132905 (2017).
- [27] A. A. Esin, A. R. Akhmatkhanov, and V. Y. Shur, Tilt control of the charged domain walls in lithium niobate, *Appl. Phys. Lett.* **114**, 092901 (2019).
- [28] H. Lu, Y. Tan, J. P. V. McConville, Z. Ahmadi, B. Wang, M. Conroy, K. Moore, U. Bangert, J. E. Shield, L. Chen, J. M. Gregg, and A. Gruverman, Electrical tunability of domain wall conductivity in LiNbO_3 thin films, *Adv. Mater.* **31**, 1902890 (2019).
- [29] B. Wolba, J. Seidel, C. Cazorla, C. Godau, A. Haußmann, and L. M. Eng, Resistor network modeling of conductive domain walls in lithium niobate, *Adv. Electron. Mater.* **4**, 1700242 (2018).
- [30] O. F. Schirmer, O. Thiemann, and M. Wohlecke, Defects in LiNbO_3 -I: experimental aspects, *J. Phys. Chem. Solids* **52**, 185 (1991).
- [31] H. J. Donnerberg, S. M. Tomlinson, and C. R. A. Catlow, Defects in LiNbO_3 -II: computer simulation, *J. Phys. Chem. Solids* **52**, 201 (1991).
- [32] E. A. Eliseev, A. N. Morozovska, G. S. Svechnikov, V. Gopalan, and V. Y. Shur, Static conductivity of charged domain walls in uniaxial ferroelectric semiconductors, *Phys. Rev. B* **83**, 235313 (2011).
- [33] V. D. Kugel and G. Rosenman, Domain inversion in heat-treated LiNbO_3 crystals, *Appl. Phys. Lett.* **62**, 2902 (1993).
- [34] T. Kämpfe, P. Reichenbach, M. Schröder, A. Haußmann, L. M. Eng, T. Woike, and E. Soergel, Optical three-dimensional profiling of charged domain walls in ferroelectrics by Cherenkov second-harmonic generation, *Phys. Rev. B* **89**, 035314 (2014).
- [35] G. Poberaj, H. Hu, W. Sohler, and P. Gunter, Lithium niobate on insulator (LNOI) for micro-photonic devices, *Laser Photonics Rev.* **6**, 488 (2012).
- [36] A. Kuroda, S. Kurimura, and Y. Uesu, Domain inversion in ferroelectric $\text{MgO}:\text{LiNbO}_3$ by applying electric fields, *Appl. Phys. Lett.* **69**, 1565 (1996).
- [37] P. Mackwitz, M. Rüsing, G. Berth, A. Widhalm, K. Müller, and A. Zrenner, Periodic domain inversion in x-cut single-crystal lithium niobate thin film, *Appl. Phys. Lett.* **108**, 152902 (2016).
- [38] M. Campbell, J. McConville, R. G. P. McQuaid, D. Prabhakaran, A. Kumar, and M. Gregg, Hall effect in charged conducting ferroelectric domain walls, *Nat. Commun.* **7**, 13764 (2016).
- [39] Y. Ohmori, M. Yamaguchi, K. Yoshino, and Y. Inuishi, Electron Hall mobility in reduced LiNbO_3 , *Jpn. J. Appl. Phys.* **15**, 2263 (1976).
- [40] D. A. Bryan, R. Gerson, and H. E. Tomaschke, Increased optical damage resistance in lithium niobate, *Appl. Phys. Lett.* **44**, 847 (1984).
- [41] W. Wang, Y. Zhong, D. Zheng, H. Liu, Y. Kong, L. Zhang, R. Romano, and J. Xu, p-type conductivity mechanism and defect structure of nitrogen-doped LiNbO_3 from first-principles calculations, *Phys. Chem. Chem. Phys.* **22**, 20 (2019).
- [42] W. Li, J. Cui, W. Wang, D. Zheng, L. Jia, S. Saeed, H. Liu, R. Rupp, Y. Kong, and J. Xu, P-type lithium niobate thin films fabricated by nitrogen-doping, *Materials (Basel)* **12**, 819 (2019).
- [43] D. A. Neamen, *Semiconductor Physics and Devices: Basic Principles* (McGraw-Hill Education, New York, 2012).
- [44] H. C. Casey, J. Muth, S. Krishnankutty, and J. M. Zavada, Dominance of tunneling current and band filling in $\text{InGaN}/\text{AlGaN}$ double heterostructure blue light-emitting diodes, *Appl. Phys. Lett.* **68**, 2867 (1996).